Journal of the Brazilian Society of Mechanical Sciences and Engineering (2021) 43:76
https://doi.org/10.1007/s40430-020-02772-x

TECHNICAL PAPER

Thermal and entropy analysis of a manifold microchannel heat sink operating on CuO–water nanofluid

Saheed Adewale Adio[1,2] · Adedotun Emmanuel Olalere[2] · Ridwan Olawale Olagoke[2] · Timothy Adefemi Alo[2] · Vasudeva Rao Veeredhi[1] · Daniel R. E. Ewim[3] · Olabode Thomas Olakoyejo[4]

Received: 24 July 2020 / Accepted: 10 December 2020

Abstract

An increase in area and disturbance of flow by introducing ribs in a microchannel system has proven to be effective in thermal management. On the other hand, nanofluid as a new coolant could also provide a much-needed performance boost. The performance of a manifold microchannel heat sink utilising nanofluid as the coolant and ribs for flow mixing has been investigated. The study is conducted with CuO–water nanofluid, Reynolds number of 100–400 and CuO nanoparticle volume fraction up to 4%. The results show that CuO–water nanofluid produced a higher thermal performance at higher concentration and Reynolds number with a corresponding increment in pressure drop. When compared to water, the Nusselt number increased from 4.4 to 23.67% at Reynolds number of 100 and CuO concentration of 4%. The addition of ribs on the sidewall of the manifold microchannel only showed a slight enhancement of up to 6.8% in the Nusselt number. Similarly, the thermal enhancement factor ranging from 1.03 to 1.07 is observed for the ribbed manifold microchannels, indicating better overall performance when compared to the microchannel without ribs.

Keywords Manifold microchannel heat sink · Nanofluids · Constant heat flux · Thermal enhancement factor

List of symbols

C_P	Specific heat capacity (m^3K/W)
D	Diameter (nm)
d_p	Nanoparticle diameter (nm)
λ	Thermal conductivity (W/mK)
H	Height of channel (nm)
W	Width of channel (nm)
Nu	Nusselt number (–)
PP	Pumping power (W)
$\dot{K}$	Flow rate (kg/s)
q''	Heat flux (W/cm^2)
Re	Reynolds number (–)
$\dot{S}$	Total entropy generation rate (W/K)
T	Temperature (K)
$\boldsymbol{V}(u,v,w)$	x, y, and z component of velocity (m/s)
X	x-axis path (m)
Y	y-axis path (m)
Z	z-axis path (m)
p	Pressure (Pa)
A	Area [$(nm)^2$]
Δp	Pressure drop (Pa)
PEC	Performance evaluation criteria (–)

Greek symbols

φ	Particle volume fraction (–)
ρ	Density (kg/m^3)
μ	Viscosity (cP)
K_b	Boltzmann constant (–)
θ	Temperature uniformity (–)
η	Thermal enhancement factor (–)

Subscripts

c	Channel
eff	Effective
f	Base fluid

Technical Editor: Ahmad Arabkoohsar.

✉ Saheed Adewale Adio
adiosa@oauife.edu.ng

✉ Daniel R. E. Ewim
daniel.ewim@tuks.co.za

[1] Department of Mechanical and Industrial Engineering, University of South Africa, Johannesburg, South Africa

[2] Department of Mechanical Engineering, Obafemi Awolowo University, Ile-Ife, Nigeria

[3] Department of Mechanical and Mechatronics Engineering, Tshwane University of Technology, Pretoria, South Africa

[4] Department of Mechanical Engineering, University of Lagos, Lagos, Nigeria

Published online: 22 January 2021

h	Hydraulic
nf	Nanofluid
o	Smooth channel
p	Nanoparticle
r	Ribbed channel

1 Introduction

Recent technological developments in manufacturing have stimulated the production of compact systems with high capabilities and functionalities. The heat generated in these systems can only be cooled within the confines of the available space, which often is not enough for proper heat dissipation. In this scenario, an effective cooling technique is becoming a necessity for the effective functioning of these high-energy devices and to avoid a reduced life span due to sudden damage resulting from excessive heat load. It has been demonstrated that microchannel heat sinks (MCHS) can achieve an efficient heat dissipation for devices and systems with extreme heat generation. An MCHS has been effective due to its high surface area-to-volume ratio; thus it possesses a high capacity to convey heat within its reduced overall size [1].

The conventional microchannel heat sink that was first introduced by Tuckerman and Pearse [1] involves a unidirectional flow and it was characterised by an elongated length in the direction of flow which is usually parallel to the base of the channel. Numerous scholars have performed detailed investigations of this type of microchannel heat sinks [2–5]; however, the major setback with the single channel—single flow microchannel is the nonuniform temperature distribution on the substrate towards the flow exit point. To stem this anomaly, some scholars have introduced porous substrates into the MCHS [6,7]. Ghahremannezhad and Vafai [6] introduced porous media into a single layer conventional microchannel heat sink to optimise it's thermal and hydraulic performance. Similarly, Ghahremannezhad et al. [8] applied porous linings into a double-layer microchannel heat sink to optimise its thermal and hydraulic performance. They discovered an optimised design for the porous thickness that improved thermal performance and the overall temperature distribution. Generally, both the conventional microchannel heat sinks and their modified versions possess good average heat transfer coefficients. Except that this is also accompanied by high pumping power as a result of the long flow length and restricted flow, resulting in a higher pressure drop [9]. To solve the problem of nonuniformity of temperature distribution, Hajmohammadi and Toghraei [10] optimised the design of a double-layered traditional MCHS utilising nanofluid as the coolant. In their work, they opined that to have a reduced thermal resistance, it is still at a high cost of pumping power due to an increase in pressure drop within the system.

Conversely, the heat transfer and pressure drop in a manifold microchannel heat sinks (MMCHS) are maximised and minimised, respectively. In an MMCHS, the flow from the inlet to the outlet remains a developing flow; thereby, enhancing mixing. Flow in a developing regime has been shown to exhibit enhanced thermal characteristics as compared to a fully developed flow [11,12]. Additionally, the MMCHS is characterised by reduced pressure drop due to shorter flow length which makes it attractive for heat transfer management in cramped spaces where pressure drop must be minimised. Harpole and Eninger [13] were part of the early researchers to show the capabilities of the MMCHS, since then, several researchers have investigated the performance and optimisation of the MMCHS [14,15]. Mandel et al. [16] studied a 2.5-D model of the MMCHS and compared it with the full 3D model, they obtained close results with the two systems. In their results, they showed that the MMCHS experiences a greater reduction in pressure at the sharp turn of the channel, and this increases as flow velocity increases. Sharma et al. [17] optimised the operating conditions of an MMCHS for processor cooling using water as the working fluid. They conducted the simulation using the single objectives and multi-objective optimisation approach. Their results showed that an inlet temperature of the coolant should be kept within 40–47.5 °C for the optimised volume flow rate of 1 l/min. Ali et al. [18] performed an experimental evaluation of three different manifold geometries; rectangular, triangular and trapezoidal manifold microchannels with a mission to achieve a higher heat transfer rate at a minimum pressure drop. Their results showed that the rectangular profile gave the highest performance among all available profiles in the laminar flow considerations. Also, for the rectangular channel, higher height, width and fin thickness of the channel was reported to increase thermal performance.

An effective approach to improving the thermal performance of a microchannel heat sink is the choice of the working fluid. In an attempt to improve the thermal property of coolant, nanoparticles with a relatively higher thermal conductivity have been dispersed in conventional heat transport fluid to produce nanofluids. Nanofluids exhibit an increased viscosity and thermal conductivity compared to the base fluid and this leads to a better thermal performance but at an increased pressure drop. Rimbault et al. [19] studied the performance of CuO–water nanofluid having a particle size of 29 nm at 0.24%, 1.03%, and 4.5% volume fractions in a microchannel heat sink. Their result proved that 1.03% volume fraction gave the best heat transfer coefficient, while 4.5% volume fraction produced an enormous pressure drop within the microchannel. On the other hand, the energetic performance coefficient was highest at 0.24%

volume fraction and lowest at 4.5%. Shi et al. [20] investigated the characteristics of AlO-water under a condition that the nanofluid concentration distribution was not uniform, thereby treating the thermophysical property of the nanofluid as anisotropic. Using this method, they showed that the heat transfer performance was improved with higher nanofluid concentration. Alfaryjat et al. [21] investigated various nanofluids in a hexagonal MCHS including ZnO-water, Al_2O_3–water, SiO_2–water, and CuO–water. From their study, Al_2O_3–water possesses the best heat transfer performance; however, CuO–water nanofluids showed the lowest pressure drop characteristics, making it suitable for low pumping power requirement. Yue et al. [22] employed Al_2O_3-water nanofluid in a manifold microchannel heat sink and their study reveals that Nusselt number is enhanced as inlet velocity and volume fraction increases. Equally, the pumping power increased with increasing flow velocity and concentration of the Al_2O_3 nanoparticles.

Fundamentally, an increased surface area could increase the heat transfer coefficient at constant heat and temperature differential. Attempts have been made based on this to increase surface area by introducing ribs in the flow path. Besides, the ribs also disrupt both the thermal and hydraulic boundary layers and enable chaotic advection of the working fluid. Several works have been done to establish an effective rib structure and to optimise existing rib structure for better thermal and hydraulic performance [23,24]. Chai and Wang [25] studied an MCHS with ribs in transverse microchambers, whose ribs utilised include forward triangular, ellipsoidal, diamond, backward triangular and rectangular ribs. About 4–31% reduction in the thermal resistance was reported. Similarly, Chai et al. [26] worked on the thermal characteristics of an MCHS with sidewalls ribs in a laminar flow regime. Rib geometries utilised include semi-circular, forward triangular, isosceles triangular, backward triangular, and rectangular ribs. The application of offset ribs showed the best thermal performance; however, the pressure drop was also maximum.

The previous experimental and numerical works [17,27] only focused on geometrical optimisation of the manifold heat sink for thermal performance enhancement. However, because they used fluid with low thermal properties, the pressure drop effect negates the gain in thermal enhancement. In this study, attempts were made to improve the overall heat transfer performance of the MMCHS using nanofluid and ribs, while improving the pressure drop. Specifically, this study is to examine the thermal, hydraulic, and thermodynamic characteristics of the MMCHS when a CuO–water nanofluid is utilised. Also, to establish the thermal performance when ribs are introduced on the microchannel sidewalls.

2 Computational domain

Figure 1a shows the MMCHS geometry, the inset A shows the base geometry computational domain for the study denoted as the smooth microchannel heat sink (S-MMCHS). To save computational power and time required for this investigation, half of the inlet to the full outlet zone has been utilized as the control volume of computation. The substrate is made of copper with constant properties. In an attempt to improve the thermal performance of the MMCHS, ribs have been introduced and attached on the inner side wall of the microchannel geometry as shown in Fig. 1b. Figure 1b shows the isometric and its corresponding front view for the rectangularly ribbed manifold microchannel heat sink (R-MMCHS). The ribs have been modelled to have the same material and properties as the base substrate. Here, four different rib geometries were proposed to study the effect of surface area and orientation on the MMCHS performance. Rib geometries include rectangular ribs (RR-MMCHS), semi-circular ribs (SC-MMCHS), forward-triangular ribs (FT-MMCHS), and backward-triangular ribs (BT-MMCHS) as shown in Fig. 1c. The geometric parameters of the MMCHS are provided in Table 1.

3 Numerical method

3.1 Governing equations and nanofluid properties

In this work, flow is laminar, steady and incompressible with a negligible effect of gravity on momentum. The nanofluid is uniformly dispersed and there is no agglomeration or sedimentation since a low volume fraction of nanoparticles has been utilised. The phases are taken to be in thermal equilibrium; hence, the flow can be treated as a single phase. Moreover, this has been validated by other researchers [28,29]. For an incompressible flow where density remains constant throughout the flow, the continuity equation is written as:

$$\nabla \cdot \left(\rho_{\text{eff}} \boldsymbol{V}\right) = 0 \tag{1}$$

The momentum equation is presented in Eq. (2).

$$\nabla \cdot \left(\rho_{\text{eff}} \boldsymbol{V}\boldsymbol{V}\right) = -\nabla p + \nabla \cdot \left(\mu_{\text{eff}} \nabla \boldsymbol{V}\right) \tag{2}$$

$\mathbf{V}$ is the velocity vector, ρ_{eff} is the nanofluid density, p is the pressure and μ_{eff} is the viscosity of the nanofluid. The energy equation for both fluid and solid domains is expressed in Eqs. (3a) and (3b), respectively.

$$\nabla \cdot \left(\rho_{\text{eff}} c_{p,\text{eff}} \boldsymbol{V} T\right) = \nabla \cdot \left(\lambda_{\text{eff}} \nabla T\right) \tag{3a}$$

$$\nabla \cdot \left(\lambda_{\text{solid}} \nabla T_{\text{solid}}\right) = 0 \tag{3b}$$

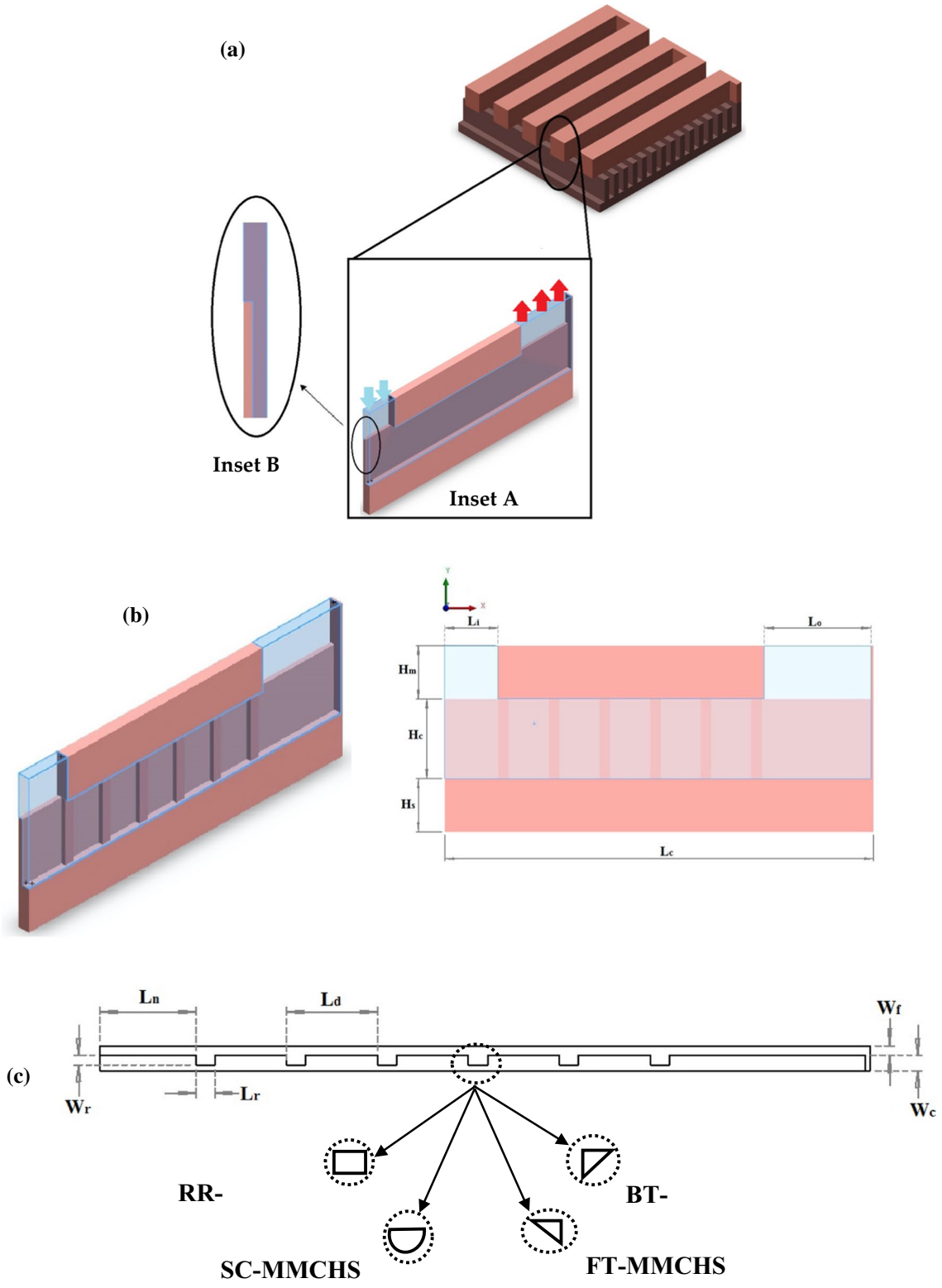

Fig. 1 The manifold microchannel heat sink and the computational geometry **a** smooth manifold microchannel heat sink **b** isometric and front views of a ribbed microchannel with the general geometric parameters **c** rib geometries and their geometric parameters

Table 1 Geometric dimensions of a unit cell of the MMCHS

Parameters	Description	Value (μm)
L_i	Length of inlet	1000
L_c	Length of channel/fin	8000
L_o	Length of outlet	2000
L_n	Distance of the first rib	1000
L_d	Rib offset	950
L_r	Rib length	280
W_r	Rib width	140
W_f	Width of fin	100
W_c	Channel width	160
H_c	Channel height	1500
H_m	Manifold height	1000
H_s	Base height	1000

where $c_{p,\text{eff}}$ is the nanofluid's specific heat capacity, T is the temperature and λ_{eff} is the thermal conductivity of the nanofluidofluid density was calculated from the physical principle of the mixture rule proposed by Xuan and Roetzel [30] and presented in Eq. (4)

$$\rho_{\text{eff}} = (1-\varphi)\rho_f + \varphi\rho_p \tag{4}$$

where subscript f and p depict the base fluid and nanoparticle, respectively. φ represents the concentration of nanoparticles in the nanofluid given by

$$\varphi = K_P/\left(K_f + K_P\right) \tag{5}$$

In Eq. (5), K denotes volume. The effective heat capacity $\left(c_p\right)_{\text{eff}}$ of nanofluid is computed by assuming thermal equilibrium within the base fluid and nanoparticles. The equation used was obtained from Khanafer and Vafai [31] and presented in Eq. (6)

$$\left(\rho c_p\right)_{\text{eff}} = (1-\varphi)\left(\rho c_p\right)_f + \varphi\left(\rho c_p\right)_p \tag{6}$$

The thermal conductivity (λ_{eff}) o) of the nanofluids obtained taking into consideration the Brownian motion and it is presented in Eqs. (7)–(11)

$$\lambda_{\text{eff}} = \lambda_{\text{static}} + \lambda_{\text{dynamic}} \tag{7}$$

The static thermal conductivity was determined using the Hamilton-crosser model while the dynamic part was obtained from the kinetic theory. Static thermal conductivity proposed by Hamilton and Crosser [32] is given in Eq. (8) and the dynamic in Eq. (9)

$$\lambda_{\text{static}} = \lambda_f\left\{\frac{\left(\lambda_p + 2\lambda_f\right) - 2\varphi\left(\lambda_f - \lambda_p\right)}{\left(\lambda_p + 2\lambda_f\right) + \varphi\left(\lambda_f - \lambda_p\right)}\right\} \tag{8}$$

Table 2 Values of constant for g-function

Constant	Values
a	−26.59331085
b	−0.403818333
c	−33.3516805
d	−1.92E+00
e	6.42E−02
m	48.40336955
h	−9.787756683
i	190.24561
j	10.92853866
k	−0.720099837

$$\lambda_{\text{dynamic}} = 5\times10^4\varphi\rho_f Cp_f\sqrt{\frac{K_b T}{d_p\rho_p}}g(T,\varphi) \tag{9}$$

$$g(T,\alpha) = \left(a + b\ln(dp) + c\ln(\varphi) + d\ln(\varphi)\ln(dp) + e\ln(dp)^2\right) \ln(T) + \left(m + h\ln(dp) + i\ln(\varphi) + j\ln(\varphi)\ln(dp) + k\ln(dp)^2\right) \tag{10}$$

The constants for the g function have been obtained semi-empirically and are given in Table 2 [33]. Recent research shows the presence of an interfacial thermal resistance which lowers the nanoparticle's thermal conductivity. Thus, the effective thermal conductivity of the nanoparticle was obtained using Eq. (11) [34]

$$R_b + \frac{d_p}{\lambda_p} = \frac{d_p}{\lambda p_{\text{eff}}} \tag{11}$$

where $R_b = 4\times10^8\frac{\text{Km}^2}{\text{W}}$.

The viscosity of the nanofluid was calculated in a similar manner using Eqs. 12–14

$$\mu_{\text{eff}} = \mu_{\text{static}} + \mu_{\text{dynamic}} \tag{12}$$

$$\mu_{\text{static}} = \frac{\mu_f}{(1-\varphi)^{2.5}} \tag{13}$$

$$\mu_{\text{dynamic}} = 5\times10^4\varphi\rho_f\sqrt{\frac{K_b T}{d_p\rho_p}}g(T,\varphi) \tag{14}$$

The thermophysical properties of the base fluid and the nanoparticles are presented in Table 3.

3.2 Numerical solution and boundary conditions

The Commercial package ANSYS FLUENT® has been utilised for solving the present heat transfer analysis. A user-defined function (UDF) was utilised in implementing the varying properties of the nanofluid, while the convergence

Table 3 Thermophysical properties of the base fluid and nanoparticle [20]

	Thermophysical properties			
	Density (kg/m^3)	Thermal conductivity (W/m K)	Specific heat (J/kg K)	Viscosity (N s/m^2)
Water	998.2	0.6	4182	0.001003
CuO	6500	20	535.6	–

criteria were kept at 10^{-6} for all considerations. The finite volume method was applied in solving the governing equations. The SIMPLEC scheme was used in coupling the pressure and the velocity fields, while the spatial discretization gradient was least-square cell-based.

At the inlet, velocity was specified as a constant value to signify a uniformly distributed inlet. A pressure outlet was applied at the outlet with gauge pressure set at zero. The heated base was subjected to a constant 100 W/cm^2 heat flux, while the symmetry boundary condition was imposed on the backside and left side of the inlet, the backside of the outlet, and the front sides of the MMCHS. Other boundaries were set to adiabatic. At all the internal walls, there exist conjugate heat transfer and a no-slip condition is imposed.

3.3 Data reduction

The Reynolds number for driving the working fluid for the analysis of this MMCHS can be written as in Eq. (15):

$$\mathrm{Re} = \frac{\rho_{\mathrm{eff}} V D_{\mathrm{h}}}{\mu_{\mathrm{eff}}} \tag{15}$$

where D_{h} is the hydraulic diameter given as

$$D_{\mathrm{h}} = \frac{2H_{\mathrm{c}}W_{\mathrm{c}}}{H_{\mathrm{c}} + W_{\mathrm{c}}} \tag{16}$$

Then, the heat transfer coefficient is stated as

$$h_{\mathrm{nf}} = \frac{\dot{q}}{T_{\mathrm{w}} - T_{\mathrm{eff}}} \tag{17}$$

where $\dot{q}$ is the heat flux, T_{w} and T_{eff} represent substrate and fluid temperatures, respectively. The nanofluid Nusselt number (Nu) is calculated from the expression in Eq. (18)

$$\mathrm{Nu} = \frac{h_{\mathrm{nf}} D_{\mathrm{h}}}{\lambda_{\mathrm{eff}}} \tag{18}$$

The pumping power which is a measure of the energy cost for driving the working fluid can be obtained using the expression in Eq. (19)

$$\mathrm{PP} = \dot{K}\Delta p \tag{19}$$

where Δp is the pressure drop and $\dot{K}$ is the volume flow rate which can be computed from the inlet area and velocity as

$$\dot{K} = v_{\mathrm{in}} A_{\mathrm{in}} \tag{20}$$

The performance evaluation criteria (PEC) is used in quantifying the compromise between the thermal and hydrodynamic performance of the nanofluid as against water. If it is greater than unit, it means the heat transfer enhancement is more than pressure drop and it can be calculated using Eq. (21)

$$\mathrm{PEC} = \frac{\mathrm{Nu}_{\mathrm{nf}}}{\mathrm{Nu}_{\mathrm{f}}} \Big/ \frac{\mathrm{PP}_{\mathrm{nf}}}{\mathrm{PP}_{\mathrm{f}}} \tag{21}$$

The thermal enhancement factor (η) has been selected to quantify the overall characteristics of the microchannel when ribs have been introduced into the system in comparison to microchannel without ribs.

$$\eta = \frac{\mathrm{Nu}_{\mathrm{R}}}{\mathrm{Nu}_{\mathrm{o}}} \Big/ \frac{\mathrm{PP}_{\mathrm{R}}}{\mathrm{PP}_{\mathrm{o}}} \tag{22}$$

Subscripts "R" represent ribbed microchannel, "nf" represents nanofluid, "o" is a smooth channel without ribs and "f" is defined earlier. Local entropy generation rate $\left(\dot{S}'''_{\mathrm{local}}\right)$ is composed of the thermal and frictional entropy as presented in Eq. (23) [29]:

$$\dot{S}'''_{\mathrm{local}} = \dot{S}'''_{\mathrm{thermal}} + \dot{S}'''_{\mathrm{frictional}} \tag{23}$$

where

$$\dot{S}'''_{\mathrm{thermal}} = \frac{\lambda_{\mathrm{eff}}}{T}\left[\left(\frac{\partial T}{\partial x}\right)^2 + \left(\frac{\partial T}{\partial y}\right)^2 + \left(\frac{\partial T}{\partial z}\right)^2\right] \tag{24a}$$

$$\dot{S}'''_{\mathrm{frictional}} = \frac{\mu_{\mathrm{eff}}}{T}\left\{\left[\left(\frac{\partial u_x}{\partial x}\right)^2 + \left(\frac{\partial u_y}{\partial y}\right)^2 + \left(\frac{\partial u_z}{\partial z}\right)^2 + \left(\frac{\partial u_x}{\partial x} + \frac{\partial u_y}{\partial y}\right)^2 + \left(\frac{\partial u_x}{\partial x} + \frac{\partial u_z}{\partial z}\right)^2 + \left(\frac{\partial u_z}{\partial z} + \frac{\partial u_y}{\partial y}\right)^2\right]\right\}. \tag{24b}$$

where $\dot{S}'''_{local}$ is the total local entropy, $\dot{S}'''_{\mathrm{thermal}}$ is the thermal entropy and $\dot{S}'''_{\mathrm{frictional}}$ is the frictional entropy generated. The over-all entropy over the whole domain is calculated using Eq. (25), while the entropy number that compares

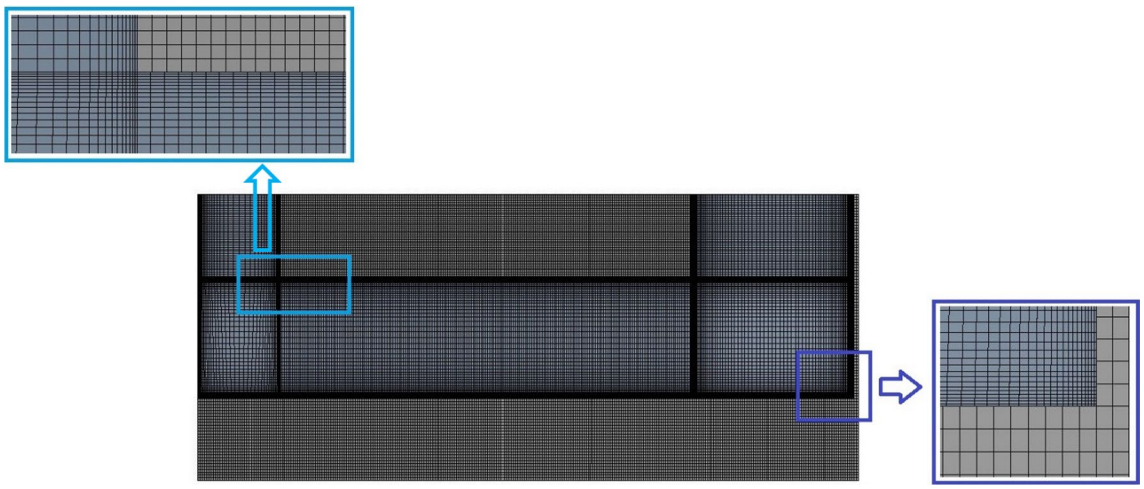

Fig. 2 The computational domain mesh structure with insets showing the refinement at the interface between the walls and the fluid

Table 4 Mesh independent study at Re = 100, $\varphi = 0.02$, $T_{in} = 300$ K

Identifier	Division factor	Elements	T_f (K)	T_{out} (K)
Case I	1 (Base division)	82,660	302.038	304.08
Case II	1.5	285,803	302.031	304.06
Case III	2	688,930	302.033	304.07
Case IV	2.5	1,315,857	302.033	304.07

the thermodynamic performance of the nanofluid in the MMCHS in comparison with water is defined by Eq. (26);

$$\dot{S}_{total} = \int \dot{S}'''_{frictional} dK + \int \dot{S}'''_{thermal} dK \tag{25}$$

$$\dot{S}_{number} = \frac{\dot{S}_{total,nf}}{\dot{S}_{total,\,f}} \tag{26}$$

4 Grid independence and validation

A structured grid was generated for the model using edge division at the three principal axes (Fig. 2). Four different grids were obtained by increasing the number of edge divisions. The base division has an element of 82,660, subsequent divisions were obtained by multiplying the base division with a factor as shown in Table 4. The grid independent study was performed at 2% concentration and Reynolds number of 100. Results were evaluated at the outlet fluid temperature and fluid average temperature as shown in Table 4. It was observed there were no changes in Case III and Case IV, therefore Case III was utilised for the simulation process.

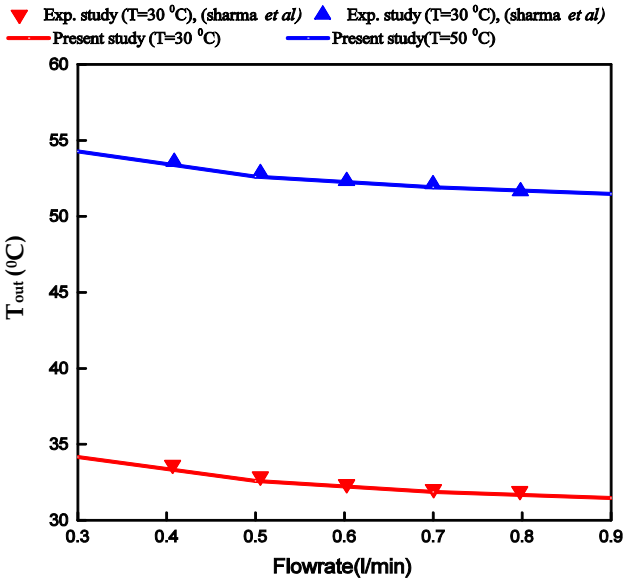

Fig. 3 Validation with the experimental result of Sharma et al. [17]

Numerical validation was conducted using the experimental result of Sharma et al. [17], numerical simulations were conducted at a flow rate of 0.3 to 0.9 l/min for inlet temperature of 30 °C and 50 °C. The heated base was subjected to a heat flux of 100 W/cm^2 for the validation. Figure 3 presents the validation of the present numerical setup with an experimental data from the open literature.

5 Results and discussion

The thermo-hydraulic and entropy characteristics of CuO–water nanofluid in a manifold microchannel heat sink was investigated using numerical approach. This work is

suited to cool electronic chips such as a CPU within small spaces. The work is carried out using various Reynolds numbers (100, 200, 300, and 400), volume fractions (0, 0.5, 1, 2, and 4%), and the addition of four different rib configurations on the microchannel sidewall. At the initial stage, the thermal and hydraulic properties of the S-MMCHS are first discussed in line with the influence of CuO concentration and the Reynolds number, and later the consequence of rib addition is discussed. General analysis of the system from the perspective of the second law of thermodynamics is presented.

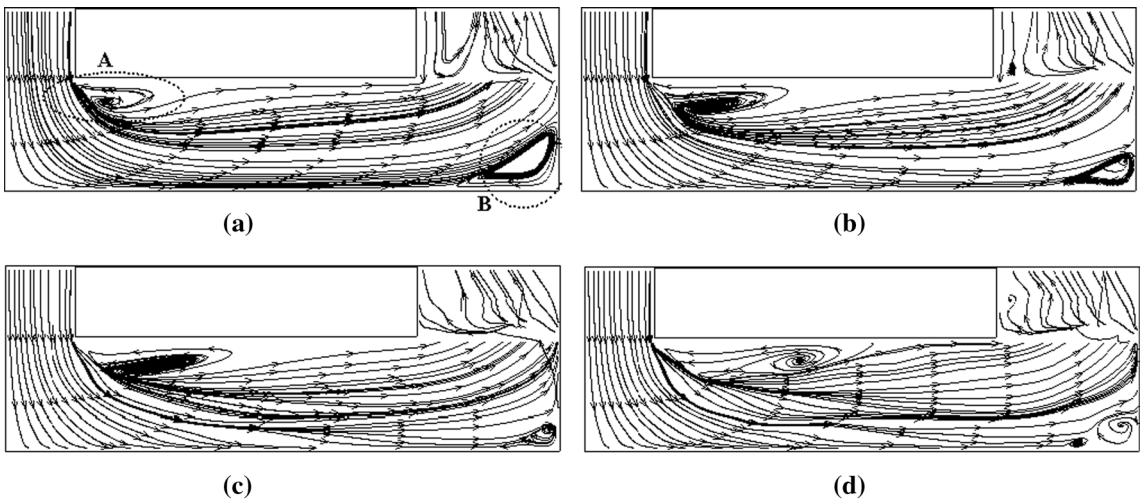

Fig. 4 Flow streamlines at $\varphi = 0.5\%$ **a** Re = 100 **b** Re = 200 **c** Re = 300 **d** Re = 400

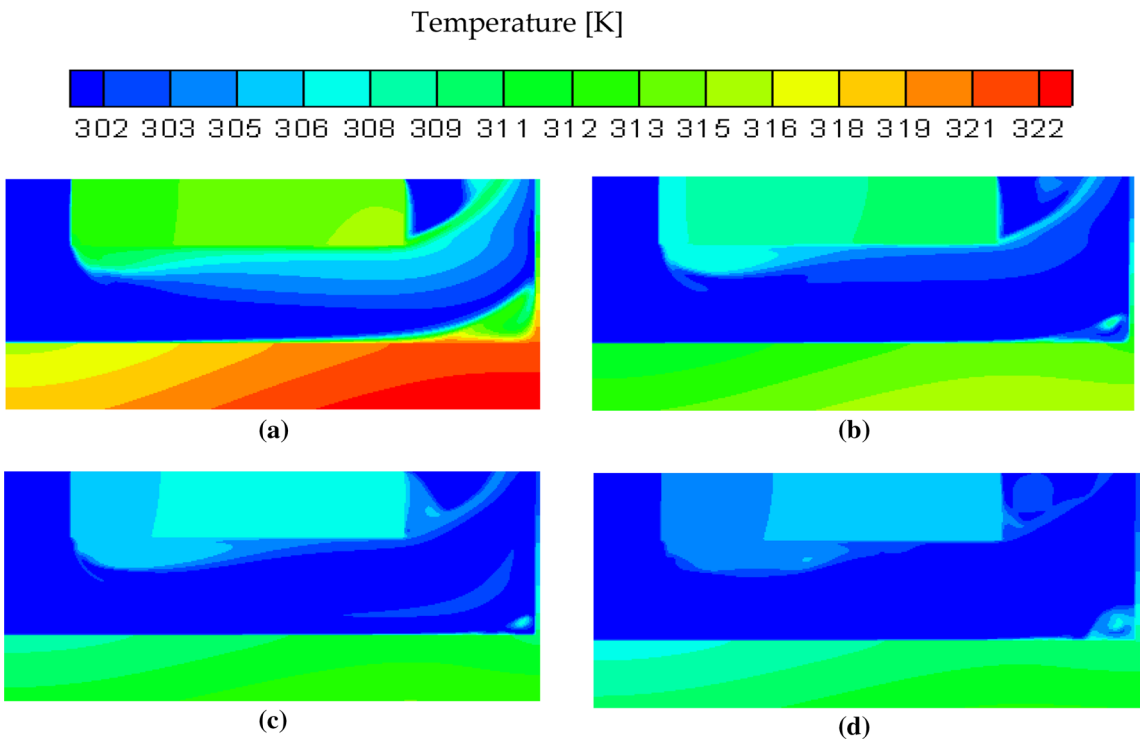

Fig. 5 Temperature distribution of the S-MMCHS at $z = 0.2$ mm and $\varphi = 0.5\%$ where **a** Re = 100 **b** Re = 200 **c** Re = 300 **d** Re = 400

5.1 Velocity, temperature and pressure characteristics

Figure 4 depicts the flow streamlines of the MMCHS at the various Reynolds numbers, while Fig. 5 represents the temperature contours for the working fluid and substrate. As the fluid flows from the inlet through the channel, there is a decrement in flow cross-sectional area (Fig. 1a inset B). The decrement in the area is accompanied by both pressure reduction and stagnated flow, these lead to an increase in the velocity between the tip of the channel and stagnation point as a result of the Bernoulli's effect (Fig. 6). The increased velocity with a low bulk temperature of the fluid at this zone is responsible for the lower substrate temperature and better cooling performance compared to that of the outlet region. As the fluid collides directly with the bottom surface of the channel there is a sudden change in direction of the fluid flow (90° counter clockwise) resulting in a change in the velocity gradient. This scenario creates the formation of vortical structures at point **A**, thus the interruption of the boundary layer formation and producing the chaotic mixing of the fluid as shown in Fig. 4. At low velocity, there is a formation of a laminar stagnation zone at point **B**. The laminar stagnation zone is known to reduce pressure drop and similarly capable of impeding heat transfer due to low conduction level at the region [26]. From Fig. 5, it can be concluded that as Reynolds number increases, the channel possesses a lower bulk temperature. Generally, for a constant heat flux, an increase in heat transfer coefficient will result in a decrease in the substrate bulk temperature. Therefore, with increasing Reynolds number there is a corresponding increase in the scale and intensity of the vortex at **A**. In this region, the disruption of the thermal boundary layer is intensified and more fluid mixing occurs with a corresponding increase in the flow disturbance along the channel length resulting in increased heat transfer coefficient. Also, it is worthy to note that an increase in the Reynolds number decreases the formation of the laminar stagnation zone at **B** thereby enhancing heat transfer characteristics and providing better thermal performance towards the exit of the channel.

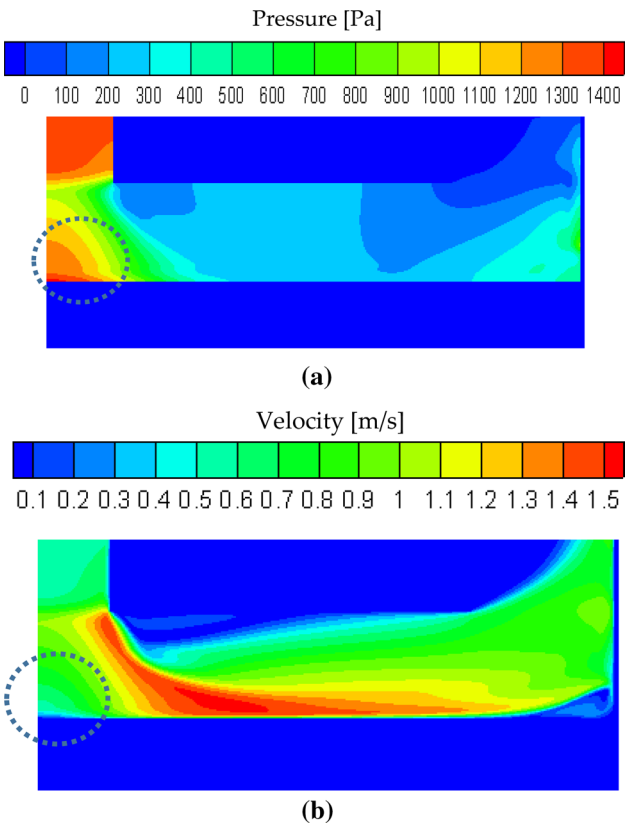

Fig. 6 Pressure and velocity contours for the S-MMCHS **a** pressure contour **b** velocity contour for $\varphi = 0.5\%$ and Re = 200

5.2 Influence of CuO concentration on the MMCHS performance

Figure 7 shows the effect of volume concentration on the temperature uniformity of the MMCHS. From the contours, using CuO–water nanofluid as the working fluid gave a better thermal performance compared to water, this is due to the superior thermal conductivity of CuO nanoparticles suspended in water. Additionally, there is micro mixing boosted by the Brownian motion of the nanoparticles and the more the nanoparticles the higher the thermal conductivity and the energy dissipation rate. This is why at a higher volume concentration of the nanoparticles, there exists a decrease in the bulk temperature of the MMCHS substrate. Moreover, heat transfer coefficient of nanofluid depends on the properties of nanoparticles alongside the interaction of the base fluid and nanoparticles [20].

The thermal performance of MCHS is improved with both increased thermal conductivity and heat transfer coefficient. Figure 7d represents a case of Re = 400 and $\varphi = 4\%$, it can be deduced that the substrate temperature is more uniform and the possibility of hotspot formation on the MMCHS substrate is less likely. This is further accentuated by the maximum substrate temperature plot presented in Fig. 8. It is evident from figure that the maximum temperature of the MMCHS reduces as Reynolds number increased, this is due to a higher heat transfer coefficient at a higher Reynolds number. Similarly, the maximum microchannel temperature decreased as the concentration of nanofluid increases. This implies that the concentration of nanoparticles at the interface of the working fluid and substrate will also increase, thereby the interfacial thermal conductivity is higher, and better heat transfer is ensured.

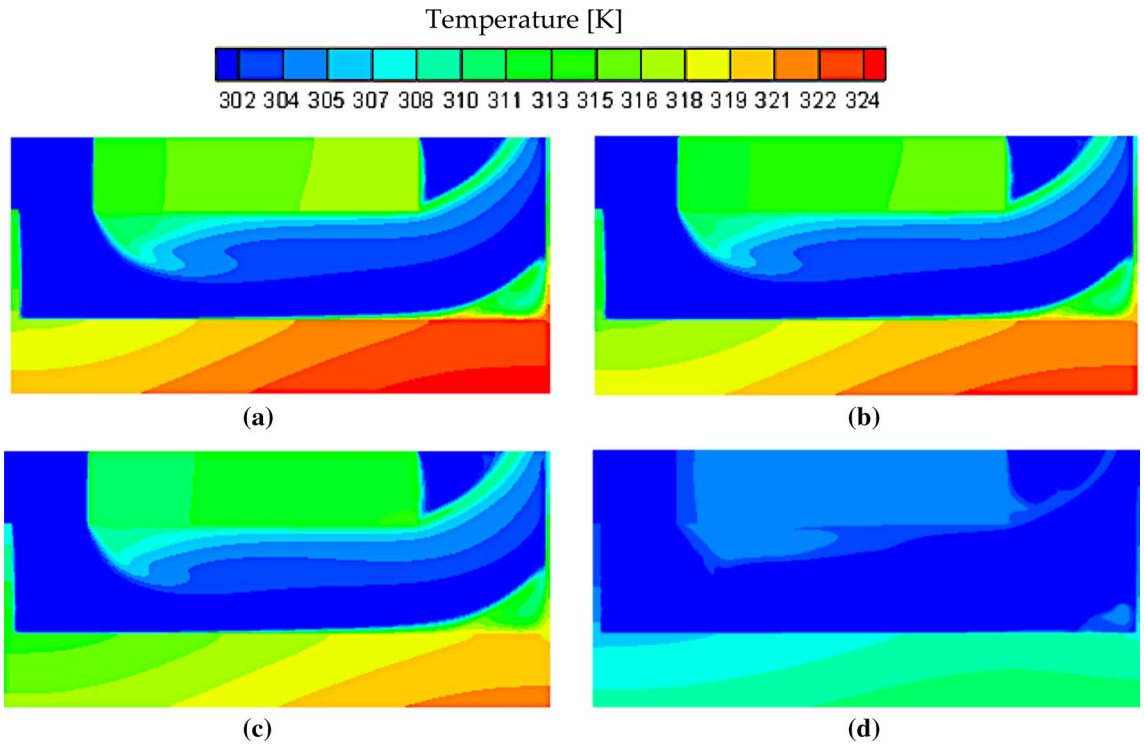

Fig. 7 Influence of CuO volume fraction on the temperature distribution of MMCHS **a** Water and Re = 100, **b** $\varphi = 0.5\%$ and Re = 100 **c** $\varphi = 4\%$ and Re = 100 and **d** $\varphi = 4\%$ and Re = 400

5.3 Nusselt number, pumping power and performance criteria

Figure 9 depicts the Nusselt number for various nanofluid concentrations and Reynolds numbers. It shows that CuO–water nanofluid gave better heat transfer performance and increasing the concentration of CuO produced an improved heat transfer performance. This is expected based on the above-mentioned superior thermal properties of nanofluid compared to water. Likewise, from Fig. 9, the Nusselt number improved as Reynolds number was increased with maximum Nusselt number values obtained at Re = 400 across all the volume fractions. In comparison with water, all the nanofluids showed improved thermal performance and there was a maximum enhancement of 23.67% for the Nusselt number at 4% concentration and Reynolds number of 100 (Fig. 9b). The Nusselt number ratio showed that CuO–water nanofluid at all the volume fractions produced better results; however, as the Reynolds number was increased the enhancement value reduced. This is primarily due to higher intensity of energy dissipation in nanofluid due to nanoparticles-fluid interactions at higher Reynolds number which was non-existent in the base fluid. Therefore, this will affect present study reveals a superior performance of CuO–water nanofluid when compared with the previous work that utilised Al_2O_3-water nanofluid [22]. Superior performance is attributed to the material property of the substrate (copper) possessing a higher thermal conductivity compared to silicon that was used by the previous author. Also, the geometric parameters of the channel used here are quite different from those found in the open literature [21] (this was optimised to obtain a better performance). Increased thermal performance when there is an increment

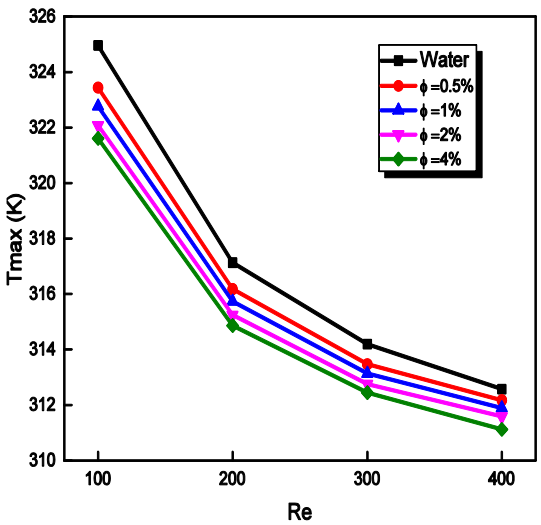

Fig. 8 Maximum substrate temperature

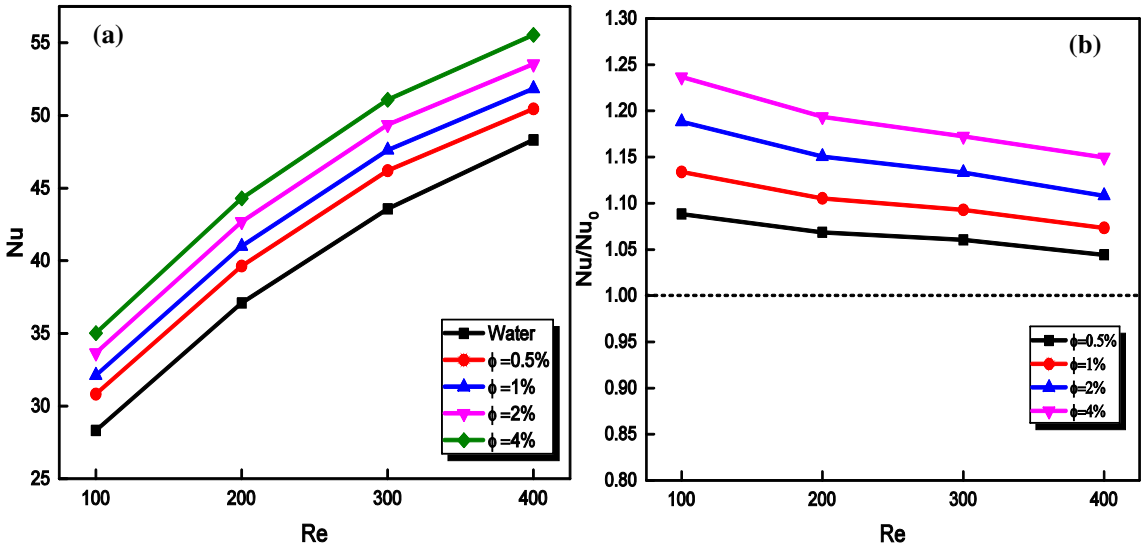

Fig. 9 Nusselt number for S-MMCHS **a** effect of Reynolds number on Nusselt number at different volume fractions **b** Nusselt number ratio at different Reynolds number and volume fractions

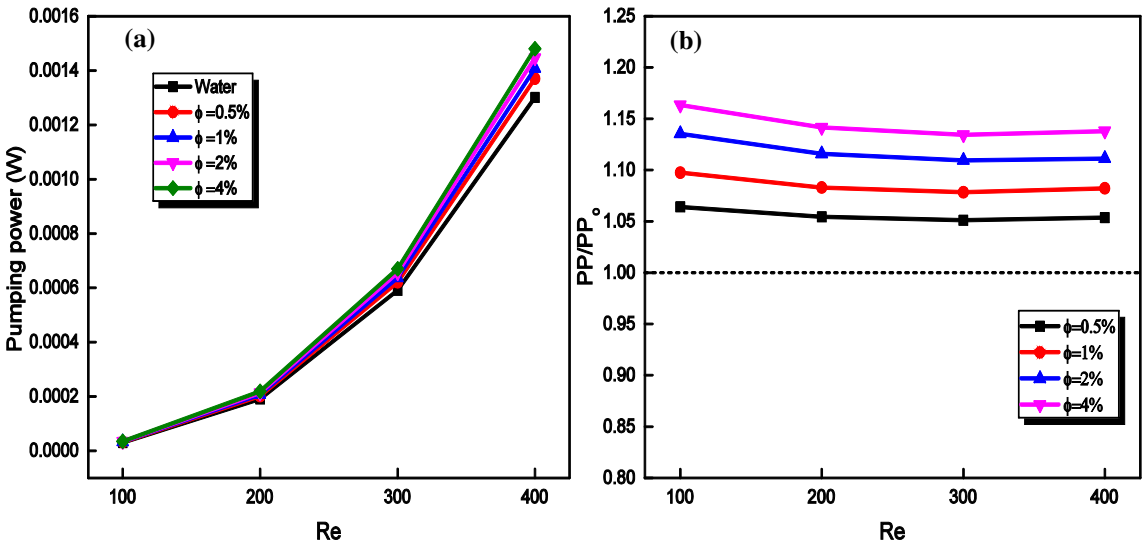

Fig. 10 Pumping power for S-MMCHS **a** pumping power at different Reynolds number and volume fractions **b** pumping power ratio at different Reynolds number and volume fractions

in channel width and channel height was previously predicted by Ali et al. [18].

The pumping power is a vital parameter to determine how cost-effective a nanofluid would be in a microchannel system. Figure 10 shows how the pumping power varies with the Reynolds number for the MMCHS at different nanofluid concentrations. It is obvious that pumping power increases with Reynolds number this is due to an increase in the inlet velocity and a corresponding increase in the pressure at the inlet zone. Higher pressure is synonymous with increased pressured drop across the microchannel therefore, the observed high pumping power at high Reynolds number. The relative pumping power shown in Fig. 10b depicts that approximately 15.2% enhancement is observed at 4% concentration and Reynolds number of 100. The Enhancements in the pumping power of CuO–water nanofluid when compared to water are as a result of the higher viscosity caused by the CuO dispersion [35–37].

Figure 11 represents the PEC for determining if the use of nanofluid is worthwhile vis á vis its thermal and pressure drop enhancements. Fundamentally, it is known that high velocity leads to higher pressure drop which can be a

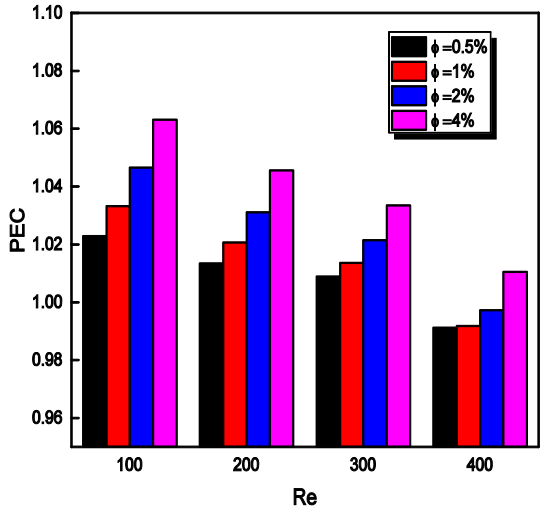

Fig. 11 Performance evaluation criteria for S-MMCHS

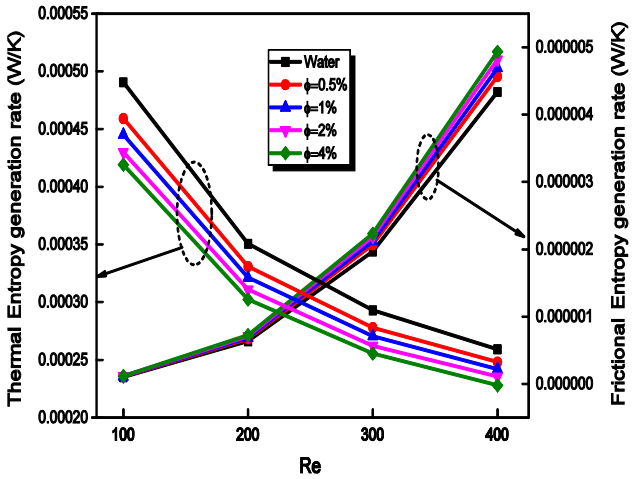

Fig. 12 Thermal and frictional entropy generation rate

considerable drawback to the thermal performance of the MMCHS. Similarly, pumping power can be enhanced when more nanoparticles are suspended. The overall performance of MMCHS (i.e. the PEC) using CuO–water nanofluid, instead of water shows a 6.5% enhancement at Re = 100 and $\varphi = 4\%$. At a higher Reynolds number, performance of the system deteriorates. This is due to a higher pressure drop associated with a high Reynolds number and higher volume fractions of CuO suspended.

5.4 Entropy generation

Entropy generation rate is used to measure the rate of irreversibility in operating the MMCHS. Irreversibility typically represents the deviation of a system from an ideal system; therefore, lower irreversibility depicts better performance. Figure 12 shows a decrease in thermal entropy $\left(\dot{S}_{\text{thermal}}\right)$ with increasing Reynolds number and nanofluid concentration. $\dot{S}_{\text{thermal}}$ deals with the measure of irreversibility occurring due to heat transfer when there is a temperature differential as presented in Eq. (24a). As Reynolds number increases, substrate temperature decreases as shown in Fig. 8, thereby resulting in a decrease in the rate of entropy generation. A similar conclusion can be made for the varying CuO concentration. $\dot{S}_{\text{frictional}}$ on the other hand, depends entirely on pressure drop; therefore, as the Reynolds number and volume fraction increase, the frictional entropy $\left(\dot{S}_{\text{frictional}}\right)$ increases. However, the magnitude of the frictional entropy is quite smaller than the thermal entropy because the MMCHS exhibits small pressure drop characteristics owing to its shorter flow length. Figure 13a shows the total entropy generation rate $\left(\left(\dot{S}_{\text{total}}\right)\right)$ in the system. The total entropy of the system follows a similar trend as the thermal entropy, chiefly because the friction entropy in the MMCHS is quite smaller than the thermal entropy. Nanofluid can be concluded to possess better thermodynamic performance than water for all Reynolds numbers and volume fractions because the entropy generation number $\left(\dot{S}_n\right)$ is less than unity for all cases studied (Fig. 13b). Also $\dot{S}_n$ increases with Reynolds number and reduces with an increase in nanofluid concentration.

5.5 Effect of rib on the performance of MMCHS

Generally, the effective mechanisms of heat transfer with the introduction of ribs include an increment in the heat transfer surface area, disruption of the thermal boundary layer, fluid acceleration due to reduction in flow area, and chaotic mixing at the region of flow separation. Figure 14 represents the maximum temperature of the microchannel's substrate for smooth and ribbed types. It was discovered that the temperature of the channel reduced depending on the type of rib used. Although there is not much difference in the performance due to the implementation of the different types of ribs, the rectangular ribbed microchannel showed the best temperature reduction. Figure 15 depicts the Nusselt number for the various geometries of the ribs at different Reynolds numbers and $\varphi = 2\%$. When compared with the smooth microchannel, it can be seen that thermal performance is higher in the ribbed microchannel at various Reynolds numbers. This is due to high intensity of the disruption of the thermal and flow boundary layer as velocity has been increased. From figure, it is evident that the rectangular ribs channel (RR-MMCHS) has the best thermal performance, while the forward triangular rib (FT-MMCHS) and backward triangular rib (BT-MMCHS) channel have very similar performance. In all cases, the ribbed microchannels performed better than the smooth microchannel

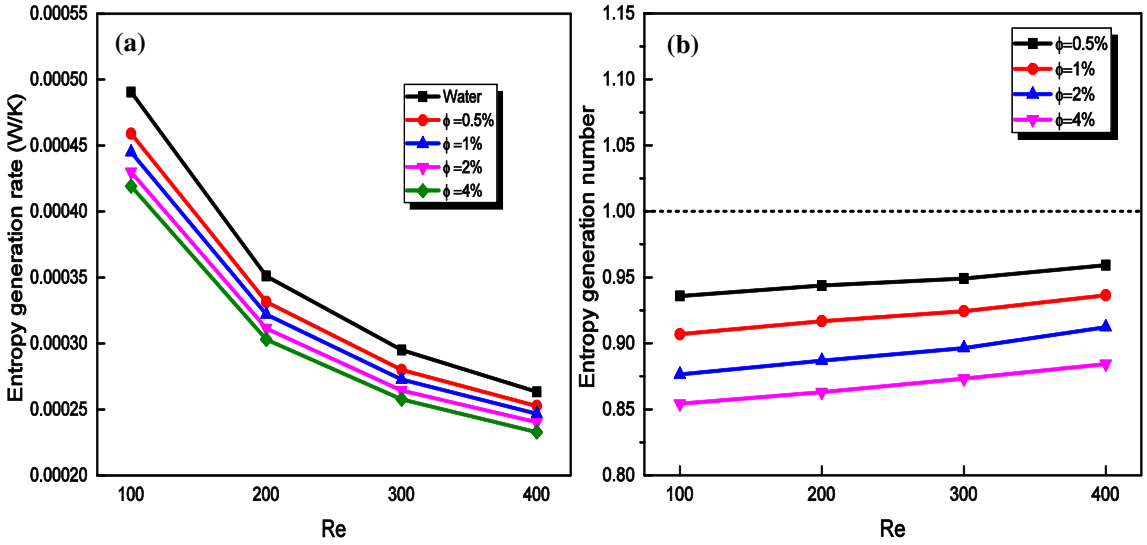

Fig. 13 The entropy generation rate and number at different Reynolds numbers **a** total entropy generation rate **b** entropy generation number

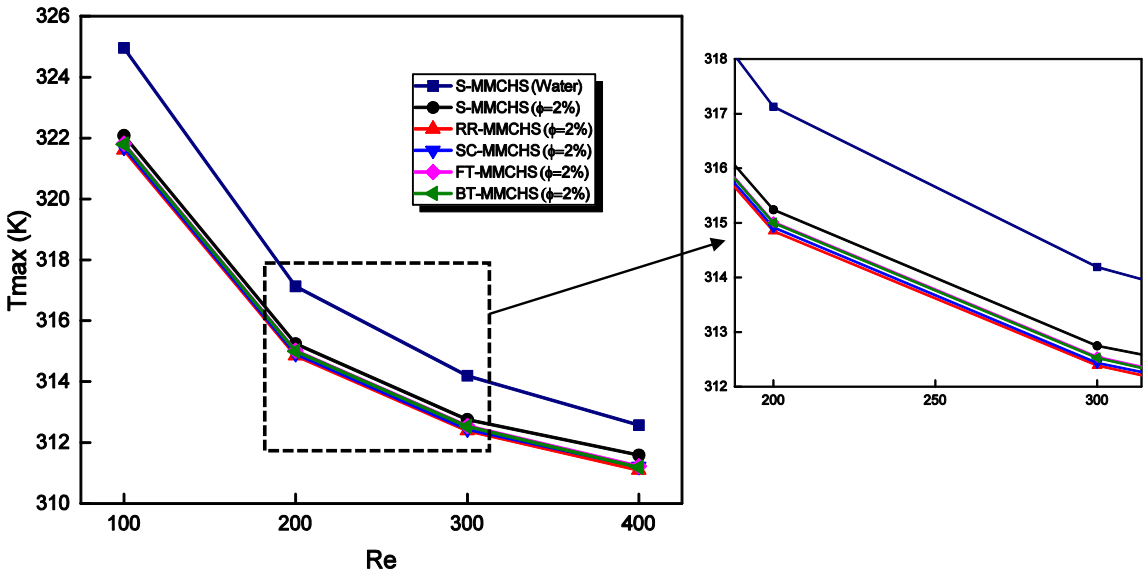

Fig. 14 Comparison of substrate temperature for the ribbed microchannels and smooth microchannel at $\varphi = 2\%$

and similar developments are obtained for other volume fractions investigated.

To comprehend the gain in thermal characteristics over the pressure drop due to the introduction of ribs, the thermal performance factor as described in Eq. (22) is presented in Fig. 16. For all the cases investigated in the present work, the microchannels with ribs proved to be better than the smooth microchannel based on rib addition. The RR-MMCHS shows the most enhancement for all the Reynolds numbers investigated. Thermal enhancement factor (η) increased with Reynolds number increase and at Re = 400, a 6.5% enhancement was obtained. Similar trends are reported for all the volume fractions investigated.

6 Conclusions

A 3D unit cell of a MMCHS has been numerically modelled to study its thermal enhancement characteristics in the laminar flow regime up to Re = 400. The impact of nanofluids at different volume fractions (φ = 0, 0.5, 1.0, 2.0, and 4.0%) and the introduction of sidewall ribs with different geometries (rectangular, forward-facing triangular,

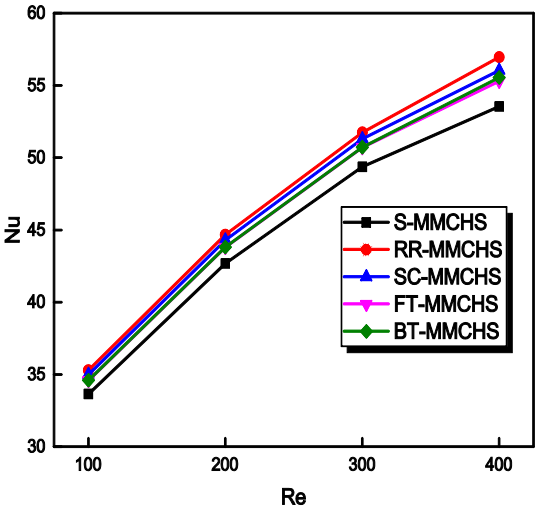

Fig. 15 Nusselt number characteristics for the ribbed microchannels and smooth microchannel at $\varphi = 2\%$

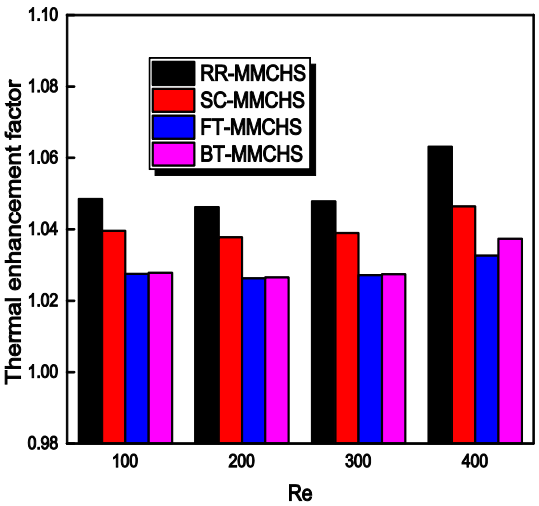

Fig. 16 Thermal enhancement factor for ribbed MMCHS at **a** $\varphi = 0.5\%$, **b** $\varphi = 1\%$, **c** $\varphi = 2\%$, **d** $\varphi = 4\%$

backwards-facing triangular and semi-circular) on the performance of a manifold microchannel has been specifically described. It was discovered that an increase in Reynolds number of improves the thermal performance and causes a high increment in pressure drop. Similarly, increasing the concentration of nanofluid increases both the thermal performance and pressure drop. CuO–water nanofluid is superior to water across all the Reynolds numbers. However, at a higher concentration of CuO nanoparticles, the high-pressure drop diminished the heat transfer gains. Introduction of ribs on sidewalls of the channel has shown to be effective in improving thermal performance, Nusselt number was found to be higher in ribbed MMCHS when compared with the smooth MMCHS. For the system with ribs, a smaller increment in pressure drop was noticed compared with the smooth MMCHS. The ribbed MMCHS offers better overall performance than the smooth MMCHS with a thermal enhancement factor greater than 1 for all rib geometries operating under the Reynolds number and nanofluid concentration considered in this study. Approximately, there is a 12% combined enhancement due to using nanofluids and ribs instead of pure water and smooth MMCHS.

Acknowledgements This research work is supported wholly/in part by the National Research Foundation of South Africa (Grant Numbers: 120710).

Compliance with ethical standards

Conflict of interest The authors of this article wish to state that no conflict of interest exit on this article.

References

1. Tuckerman DB, Pease RFW (1981) High-performance heat sinking for VLSI. IEEE Electron Dev Lett EDL 2:126–129. https://doi.org/10.1109/EDL.1981.25367
2. Mohammed HA, Gunnasegaran P, Shuaib NH (2010) Heat transfer in rectangular microchannels heat sink using nanofluids. Int Commun Heat Mass Transf 37:1496–1503. https://doi.org/10.1016/j.icheatmasstransfer.2010.08.020
3. Ebrahim S, Ranjbar AA, Hosseini MJ (2017) Experimental and numerical investigation of circular minichannel heat sinks with various hydraulic diameter for electronic cooling application. Microelectron Reliab 73:97–105. https://doi.org/10.1016/j.microrel.2017.04.028
4. Manay E, Feyza E, Sahin B (2018) Entropy generation of nanofluid flow in a microchannel heat sink. Results Phys 9:615–624. https://doi.org/10.1016/j.rinp.2018.03.013
5. Sheikhalipour T, Abbassi A (2018) Numerical analysis of nanofluid flow inside a trapezoidal microchannel using different approaches. Adv Powder Technol. https://doi.org/10.1016/j.apt.2018.04.010
6. Ghahremannezhad A, Vafai K (2018) Thermal and hydraulic performance enhancement of microchannel heat sinks utilizing porous substrates. Int J Heat Mass Transf 122:1313–1326. https://doi.org/10.1016/j.ijheatmasstransfer.2018.02.024
7. Gong L, Li Y, Bai Z, Xu M (2018) Thermal performance of micro-channel heat sink with metallic porous/solid compound fin design. Appl Therm Eng. https://doi.org/10.1016/j.applthermaleng.2018.03.065
8. Ghahremannezhad A, Xu H, Alhuyi M, Hossein M, Vafai K (2019) Effect of porous substrates on thermohydraulic performance enhancement of double layer microchannel heat sinks. Int J Heat Mass Transf 131:52–63. https://doi.org/10.1016/j.ijheatmasstransfer.2018.11.040
9. Arie MA, Shooshtari AH, Dessiatoun SV, Al-Hajri E, Ohadi MM (2015) Numerical modeling and thermal optimization of a single-phase flow manifold-microchannel plate heat exchanger. Int J Heat Mass Transf 81:478–489. https://doi.org/10.1016/j.ijheatmasstransfer.2014.10.022
10. Hajmohammadi MR, Toghraei I (2018) Optimal design and thermal performance improvement of a double-layered microchannel

heat sink by introducing Al_2O_3 nano-particles into the water. Phys A 505:328–344. https://doi.org/10.1016/j.physa.2018.03.040
11. Xu JL, Gan YH, Zhang DC, Li XH (2005) Microscale heat transfer enhancement using thermal boundary layer redeveloping concept. Int J Heat Mass Transf 48:1662–1674. https://doi.org/10.1016/j.ijheatmasstransfer.2004.12.008
12. Dewan A, Srivastava P (2015) A review of heat transfer enhancement through flow disruption in a microchannel. J Therm Sci 24:203–214. https://doi.org/10.1007/s11630-015-0775-1
13. Harpole GM, Eninger JE (1991) Micro-channel heat exchanger optimization. In: 1991 proceedings, seventh IEEE semiconductor thermal measurement and management symposium. IEEE, pp 59–63
14. Boteler L, Jankowski N, McCluskey P, Morgan B (2012) Numerical investigation and sensitivity analysis of manifold microchannel coolers. Int J Heat Mass Transf 55:7698–7708. https://doi.org/10.1016/j.ijheatmasstransfer.2012.07.073
15. Drummond KP, Back D, Sinanis MD, Janes DB, Peroulis D, Weibel JA, Garimella SV (2018) A hierarchical manifold microchannel heat sink array for high-heat-flux two-phase cooling of electronics. Int J Heat Mass Transf 117:319–330. https://doi.org/10.1016/j.ijheatmasstransfer.2017.10.015
16. Mandel R, Shooshtari A, Ohadi M (2018) A "2.5-D" modeling approach for single-phase flow and heat transfer in manifold microchannels. Int J Heat Mass Transf 126:317–330. https://doi.org/10.1016/j.ijheatmasstransfer.2018.04.145
17. Sharma CS, Zimmermann S, Tiwari MK, Michel B, Poulikakos D (2012) Optimal thermal operation of liquid-cooled electronic chips. Int J Heat Mass Transf 55:1957–1969. https://doi.org/10.1016/j.ijheatmasstransfer.2011.11.052
18. Ali MA, Khan TS, Al Hajri E (2016) Numerical simulation of manifold microchannel heat exchanger. In: Proceedings of the ASME 2016 international mechanical engineering congress and exposition (IMECE2016-66960), pp 1–10
19. Rimbault B, Tam C, Galanis N (2014) Experimental investigation of CuO e water nano fl uid fl ow and heat transfer inside a microchannel heat sink. Int J Therm Sci 84:275–292. https://doi.org/10.1016/j.ijthermalsci.2014.05.025
20. Shi X, Li S, Wei Y, Gao J (2018) Numerical investigation of laminar convective heat transfer and pressure drop of water-based Al_2O_3 nanofluids in a microchannel. Int Commun Heat Mass Transf 90:111–120. https://doi.org/10.1016/j.icheatmasstransfer.2017.11.007
21. Alfaryjat AA, Mohammed HA, Adam NM, Stanciu D, Dobrovicescu A (2018) Numerical investigation of heat transfer enhancement using various nanofluids in hexagonal microchannel heat sink. Therm Sci Eng Prog 5:252–262. https://doi.org/10.1016/j.tsep.2017.12.003
22. Yue Y, Mohammadian SK, Zhang Y (2015) Analysis of performances of a manifold microchannel heat sink with nano fluids. Int J Therm Sci 89:305–313. https://doi.org/10.1016/j.ijthermalsci.2014.11.016
23. Adewumi OO, Bello-Ochende T, Meyer JP (2017) Numerical investigation into the thermal performance of single microchannels with varying axial length and different shapes of micro pin-numerical investigation into the thermal performance of single microchannels with varying axial length and different. Heat Transf Eng. https://doi.org/10.1080/01457632.2016.1239927
24. Wang R, Wang J, Lijin B, Zhu Z (2018) Parameterization investigation on the microchannel heat sink with slant rectangular ribs by numerical simulation. Appl Therm Eng 133:428–438. https://doi.org/10.1016/j.applthermaleng.2018.01.021
25. Chai L, Wang L (2018) Thermal-hydraulic performance of interrupted microchannel heat sinks with di ff erent rib geometries in transverse microchambers. Int J Therm Sci 127:201–212. https://doi.org/10.1016/j.ijthermalsci.2018.01.029
26. Chai L, Dong G, Sheng H (2016) Numerical study of laminar flow and heat transfer in microchannel heat sink with offset ribs on sidewalls. Appl Therm Eng 92:32–41. https://doi.org/10.1016/j.applthermaleng.2015.09.071
27. Sharma CS, Tiwari MK, Michel B, Poulikakos D (2013) Thermofluidics and energetics of a manifold microchannel heat sink for electronics with recovered hot water as working fluid. Int J Heat Mass Transf 58:135–151. https://doi.org/10.1016/j.ijheatmasstransfer.2012.11.012
28. Baïri a., Zarco-Pernia E, García De María JM, (2014) A review on natural convection in enclosures for engineering applications. the particular case of the parallelogrammic diode cavity. Appl Therm Eng 63:304–322. https://doi.org/10.1016/j.applthermaleng.2013.10.065
29. Al-Rashed AAAA, Shahsavar A, Entezari S, Moghimi MA, Adio SA, Nguyen TK (2019) Numerical investigation of non-Newtonian water-CMC/CuO nanofluid flow in an offset strip-fin microchannel heat sink: thermal performance and thermodynamic considerations. Appl Therm Eng 155:247–258. https://doi.org/10.1016/j.applthermaleng.2019.04.009
30. Xuan Y, Roetzel W (2000) Conceptions for heat transfer correlation of nanofluids. Int J Heat Mass Transf 43:3701–3707. https://doi.org/10.1016/S0017-9310(99)00369-5
31. Khanafer K, Vafai K (2011) A critical synthesis of thermophysical characteristics of nanofluids. Int J Heat Mass Transf 54:4410–4428. https://doi.org/10.1016/j.ijheatmasstransfer.2011.04.048
32. Hamilton R, Crosser O (1962) Thermal conductivity of heterogeneous two-component systems. Ind Eng Chem 1:187–191. https://doi.org/10.1021/i160003a005
33. Li J (2008) Computational analysis of nanofluid flow in microchannel with application to micro-heat sinks and BIO-MEMS
34. Jang SP, Choi SUS (2013) Effects of various parameters on nanofluid thermal conductivity. J Heat Transf. https://doi.org/10.1115/1.2712475
35. Adio SA, Sharifpur M, Meyer JP (2015) Investigation into effective viscosity, electrical conductivity, and pH of γ-Al_2O_3-glycerol nanofluids in Einstein concentration regime. Heat Transf Eng. https://doi.org/10.1080/01457632.2015.994971
36. Sharifpur M, Adio SA, Meyer JP (2015) Experimental investigation and model development for effective viscosity of Al_2O_3-glycerol nanofluids by using dimensional analysis and GMDH-NN methods. Int Commun Heat Mass Transf 68:208–219. https://doi.org/10.1016/j.icheatmasstransfer.2015.09.002
37. Awua JT, Ibrahim JS, Adio SA, Mehrabi M, Sharifpur M, Meyer JP (2018) Experimental investigations into viscosity, pH and electrical conductivity of nanofluid prepared from palm kernel fibre and a mixture of water and ethylene glycol. Bull Mater Sci 41:156. https://doi.org/10.1007/s12034-018-1676-1